Rapid porosity and permeability changes of calcareous sandstone due to CO$_2$-enriched brine injection

Benoit Lamy-Chappuis[1], Doug Angus[1], Quentin Fisher[1], Carlos Grattoni[1], and Bruce W. D. Yardley[1]

[1]School of Earth and Environment, University of Leeds, Leeds, UK

Abstract Reservoir injectivity and storage capacity are the main constraints for geologic CO$_2$ sequestration, subject to safety and economic considerations. Brine acidification following CO$_2$ dissolution leads to fluid-rock interactions that alter porosity and permeability, thereby affecting reservoir storage capacity and injectivity. Thus, we determined how efficiently CO$_2$-enriched brines could dissolve calcite in sandstone cores and how this affects the petrophysical properties. During computerized tomography monitored flow-through reactor experiments, calcite dissolved at a rate largely determined by the rate of acid supply, even at high flow velocities which would be typical near an injection well. The porosity increase was accompanied by a significant increase in rock permeability, larger than that predicted using classical porosity-permeability models. This chemically driven petrophysical change might be optimized using injection parameters to maximize injectivity and storage.

1. Introduction

Carbon dioxide storage in geological formations such as saline aquifers or depleted oil or gas fields is viewed as a potentially effective means to mitigate global warming [*Bachu et al.*, 1994; *IEA*, 2010; *IPCC*, 2005]. Among the 29 Gt of anthropogenic CO$_2$ emitted globally per year, 60% originates from large stationary sources [*Oelkers and Cole*, 2008]; this represents a considerable target for carbon capture and storage technology. Saline aquifers are of particular interest due to their abundance and their storage potential [*Bachu and Adams*, 2003]. A striking feature is the great variability in the fundamental properties of these reservoirs, including geometry, pressure, temperature, porosity, permeability, and mineralogical composition. Previous experimental studies [*Bateman et al.*, 2011; *Rosenbauer et al.*, 2005], numerical modeling studies [*Andre et al.*, 2007; *Knauss et al.*, 2005], and field studies [*Kharaka et al.*, 2006] indicated that significant rock alteration could follow CO$_2$ injection, involving simple mineral dissolution or more complex dissolution-precipitation reactions.

Reaction modification of permeability and porosity can be of great importance for reservoir screening and injection design. To predict changes in permeability caused by fluid-rock interactions, reactive transport codes like TOUGHREACT [*Xu et al.*, 2011] include permeability-porosity relationships. These equations reproduce porosity and permeability trends with depth due to compaction, but during reactive transport, changes in the pore structure may be localized at specific sites linked to mineral distribution. Thus, porosity-permeability relationships optimized for continuous variations of natural rocks may not reproduce the continuum scale effect of local chemical reactions. An example is the wormholing of limestone [*Luquot and Gouze*, 2009]. Added complexity stems from the possibility that the release of fines, secondary precipitation, clay swelling, and enhanced compaction may lead to contradictory permeability-porosity relationships [*Bowker and Shuler*, 1991; *Sayegh et al.*, 1990; *Yu et al.*, 2012].

This experimental study explores the effects of mineral dissolution in response to CO$_2$ injection on the porosity and permeability of a rock containing a small fraction of dispersed shell fragments.

2. Experimental Method

A flow-through reactor was used to inject CO$_2$-saturated brine into rock cores (Figure 1) and was instrumented to monitor fluid chemistry and permeability. Rock cores were initially saturated with brine and stored for at least 2 days before being loaded into the core holder. Once the experiment started, the initial brine was displaced by
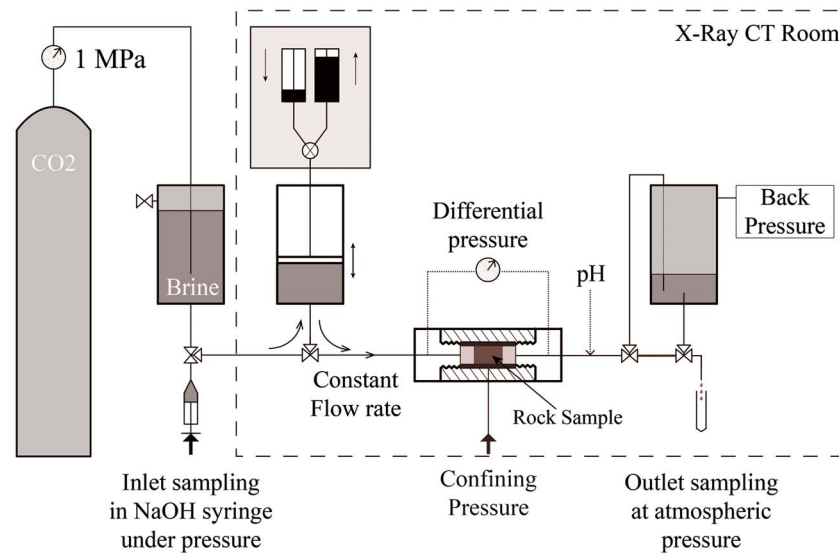
Figure 1. Overview of the experimental setup. CO_2–saturated brine was stored above a floating piston and injected into the rock sample via a Quizix® dual pump system (dark gray box). The core holder was placed in the CT scanner during the entire course of the experiment.

CO_2-saturated brine, and porosity evolution was monitored periodically with time-lapse computerized tomography (CT) scanning using a PICKER PQ 2000 medical CT scanner (pixel resolution: 250 µm), which detects changes in density.

In a set of six experiments, we injected CO_2-saturated brines at constant flow rates (1, 2, or 3 mL min^{-1}), for 1 or 2 days, to mimic conditions near the CO_2-brine interface as it migrates away from the injection well. The injected fluid was 1 M NaCl brine, normally saturated under 1 MPa CO_2 pressure at room temperature (CO_2 concentration $= 0.3$ mol L^{-1}, pH $= 3.3$). The inlet pore pressure of 1 MPa was selected because it is the maximum pressure for operation of the Unisense® pH electrode (Figure 1). During supercritical CO_2 injection in deep saline aquifers, CO_2 solubility will typically be between 0.7 and 1.2 mol L^{-1}, and the pH at the CO_2-brine interface could be as low as 2.8. The differential pressure was monitored, and changes in permeability during each run was calculated from Darcy's law (the Reynolds number for our experiments was 0.001–0.004). The accurate measurements of permeability were performed under pure brine-saturated conditions before and after the experiments to avoid possible uncertainty due to degassing.

3. Sample Description

Cylindrical cores (5 cm long and 3.75 cm in diameter) were drilled parallel to bedding from a single sample block of Jurassic Lower Calcareous Gritstone Formation from Cayton Bay, Scarborough (UK). Initial porosity of 30.5 to 35.5% (average 33%) was measured with both helium expansion and NMR (nuclear magnetic resonance) methods. NMR analyses showed a bimodal pore size distribution with a main peak at 100 µm. Scanning electron microscope (SEM) observations show that the rock contains numerous round pores, 100 µm in diameter, but these are connected by small-pore throats. Initial permeability of the cores ranged from 8 to 12 mdarcy, i.e., at the low end of the permeabilities encountered in current injection projects [*Michael et al.*, 2010].

Mineral composition was determined by quantitative X-ray diffraction (QXRD), and element maps were also acquired using a scanning electron microscope mounted with an energy dispersive X-ray spectrometer on polished thin sections. Total inorganic carbon analyses were performed on five subsamples to capture the range of calcite contents. Calcite comprised 4–5% of the rock mass and was in the form of isolated grains and bioclast fragments. Thus, about 4.5% of the rock mass (3% of its total volume) could quickly dissolve in acid, provoking pore network modifications. The remainder of the solid material was comprised of quartz (76% by mass), muscovite (7.5%), microcline (6.5%), illite/smectite (2.5%), kaolinite (1%), albite (1%), dolomite (0.7%), and pyrite (0.5%).
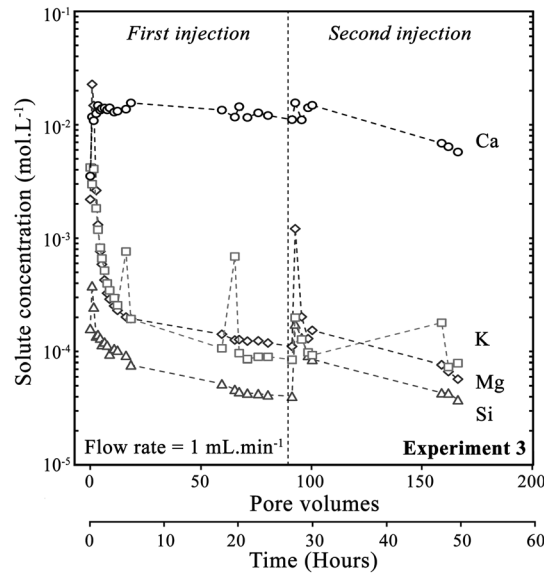
Figure 2. Breakthrough curves from experiment 3. The separation line marks a 4 h break between the first and the second injection of CO_2-saturated brine. The concentrations of most elements drop due to dilution by newly injected brine, but Ca concentrations remain quite stable due to calcite dissolution.

4. Fluid Chemistry

Samples of acidified brine were collected under working pressure (1 MPa) at the inlet prior to injection and analyzed for the total CO_2 by titration to verify the CO_2 concentration of the injected fluid against expected values [*Duan and Sun*, 2003]. Outflow sampling was done at intervals of 15 min at the beginning of the experiment, then less frequently. Additionally, the pH was continuously monitored at the outlet using a small-volume electrode system described by *Rosenqvist et al.* [2012]. Breakthrough curves for cations from experiment 3 are shown in Figure 2; results for experiments 1 and 6 are shown in Figure S1 of the Supporting Information.

Analyses of the effluent fluids indicate that calcite dissolution dominated in each experiment. For experiment 3 (Figure 2), integration of the curves indicates leaching of 37.0, 1.0, 0.7, and 0.2 mmol of Ca, Mg, K, and Si, respectively, corresponding to the dissolution of 3.66 g calcite and 0.21 g dolomite with minor silicates. The equivalent volumes are 1.36 and 0.07 cm^3, yielding a total of 1.43 cm^3 if there was no secondary precipitation. This is thought unlikely as calcium was steadily released throughout the experiments and pH dropped progressively. These changes calculated from effluent composition correspond well with the changes in core mass and pore volume measured by mass balance and helium porosimetry of 4.24 g and 1.78 cm^3, respectively. During the initial stages of the experiment, the pH of the inlet fluid was 3.3, while the outlet pH was 7.5, reflecting extensive reaction of calcite and mixing with initial pore fluid (pH 9.5). The outlet pH dropped throughout the experiments and, by the end of each experiments, was very close to the inlet value. The gradual drop in pH is inferred to result from the development of preferential flow paths through the core from which calcite was completely dissolved at an early stage, while some calcite remained along the other flow paths. The measured pH of the fluid exiting the core is believed to reflect mixing of reacted and unreacted brine from calcite-rich and calcite-free flow paths. Because of the development of calcite-free flow paths, twice as much fluid was injected than was required to dissolve all the calcite at 100% efficiency. QXRD analyses of subsamples taken from the inlet and the center of the core after experiment 3 showed the total removal of calcite, with no other mineralogical changes. About 25% of the initial calcite remained at the far end of the core; hence, outflow calcium concentrations remain significant, although falling, indicating that calcite dissolution was close to completion.

5. Dissolution Front Tracking

A time series of CT profiles of the core (each comprising 24 slices perpendicular to the core axis) were used to track the dissolution front as it migrated during the course of each experiment. Results for experiment 3 are shown in Figure 3. Initial and final porosity profiles were calculated using

$$\phi = (CT_{bs} - CT_{as}) / (CT_b - CT_a), \tag{1}$$

where ϕ is the porosity of a core slice and CT_{bs} and CT_{as} are the averaged CT value of the pixels comprising the slice, under 100% brine saturation and 100% air saturation, respectively. CT_b and CT_a are the CT values of pure brine and air [*Withjack*, 1988].

If a single mineral is dissolving (or multiple minerals with similar X-ray attenuation coefficients) then

$$\delta_{CT} = \delta_\phi (CT_b - CT_{mineral}), \tag{2}$$

since $CT_b - CT_{mineral}$ is a constant, the variation in porosity (δ_ϕ) is directly proportional to the variation of the CT number (δ_{CT}). This equation was used to calculate intermediate porosity profiles (Figure 3).
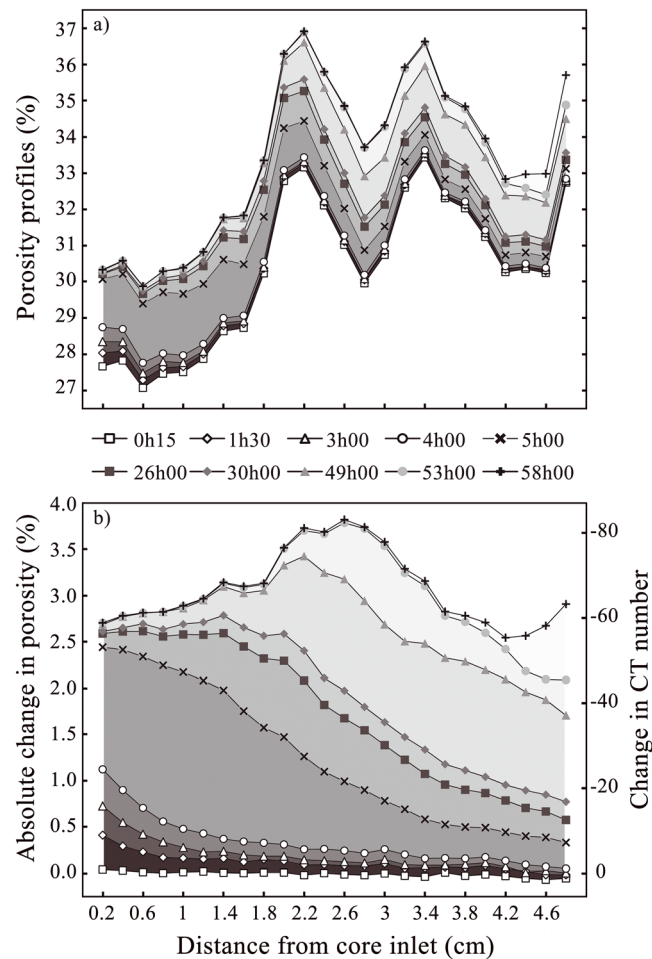
Figure 3. Time series to demonstrate porosity evolution in experiment 3. Together with experimental data points, (a) time-lapse porosity profiles are presented as surfaces of decreasing gray scale intensity. They have been normalized to the (b) initial porosity profile. Equivalence with change in CT number (in Hounsfield units [*Hounsfield*, 1973]) is also shown.

Near the inlet, there was a rapid porosity increase at the start of the experiment; approximately half the porosity increase occurred in the first 5 h and 90% within 18 h. This is likely due to rapid dissolution of more accessible calcite grains. With time, the region of rapid dissolution propagated down the core, and extensive porosity increase at the outflow began only after 18 h had elapsed. This pattern of migration of the zone of dissolution demonstrates that dissolution was transport limited even at the low CO_2 concentration and high flow velocities of these experiments. The Damköhler number calculated for calcite dissolution during flow and averaged over the core length ranged from 19 to 24, while the Péclet number was between 6 and 18 (Table S1 of the Supporting Information provides the details). Thus, although the dissolution of calcite was not 100% efficient due to the development of calcite-free pathways, these results validate the use of the local equilibrium assumption for simulations of calcite dissolution at the reservoir scale and demonstrate that it is the physical introduction of acidity to calcite-bearing rocks that will dictate how much calcite dissolves, rather than surface reaction rates, as shown for pure calcite by *Pokrovsky et al.* [2005].

6. Influence of Mineral Dissolution on Porosity and Permeability

Six similar dissolution experiments were performed on samples with variable amounts of calcite, and in each case, injection was stopped only after the permeability and the outlet pH had stabilized. At this stage, the outlet pH was close to the inlet pH indicating little reaction in the flow paths controlling the permeability. Permeability and pH data for three experiments at different flow rates are presented in Figure 4. The relative increase in porosity resulting from dissolution in the cores ranged from 5 to 15%. Note however that no net
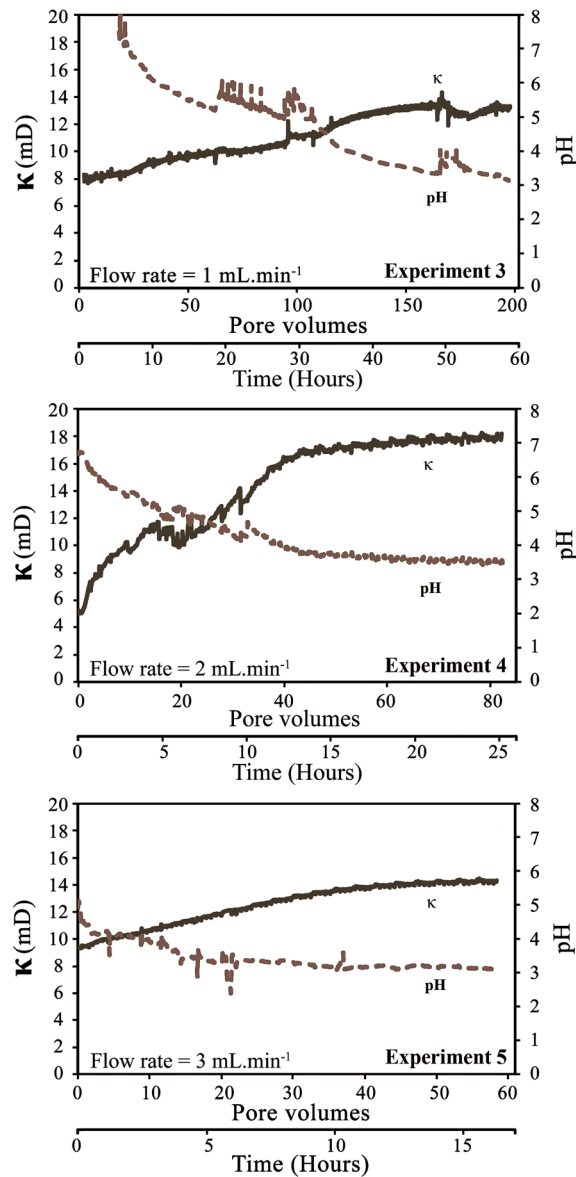
Figure 4. Permeability and pH curves for experiments 3, 4, and 5. The time needed for the permeability and the pH to stabilize is strongly correlated to the flow rate, demonstrating that the rate of calcite dissolution is transport limited. Note that the initial permeability for the core used in experiment 4 measured with pure brine was 10.2 mdarcy, and this value was used for the calculation of permeability change in Figure 5. It differs from the value measured early in the run shown in this figure. This is the only inconsistency encountered in all the six experiments and is most likely due to the presence of gaseous CO_2 in the pipes at the start of the experiment.

gain of porosity should occur at the field scale as calcite will mostly reprecipitate away from the region exposed to high CO_2 pressure. Figure 5 is a porosity-permeability plot showing the increase in porosity and permeability for each experiment and demonstrates a marked increase in permeability. Not only can dissolution increase storage capacity through porosity redistribution, it can also significantly increase permeability and hence improve CO_2 injectivity. This is particularly significant in low-permeability reservoirs where the injection pressure limits the injection rate.

We attempted to fit our experimental data to the Kozeny-Carman (K-C) reference equation for the relation between permeability (κ) and porosity (ϕ) [*Bear*, 1972]:

$$\kappa \propto \phi^n / (1 - \phi)^2, \tag{3}$$

where n ranges from 3 to 7, and the modified Kozeny-Carman equation of *Mavko et al.* [2003]:
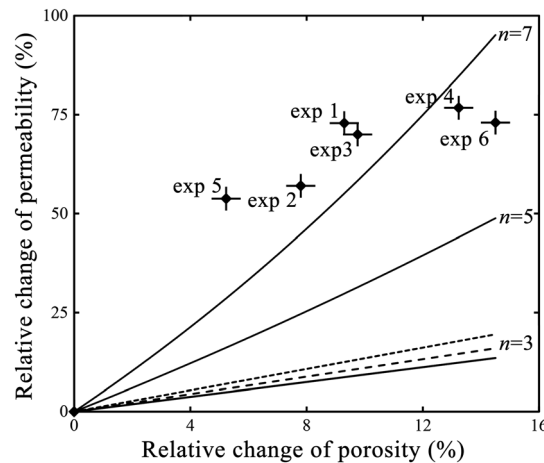
Figure 5. Relative changes of porosity and permeability for six experiments (experiment numbers are displayed next to data points). Also shown is the calculated permeability change for each measured porosity change, based on different parameterizations ($\phi_{critical}$ and n, see text) of the Kozeny-Carman equation. Solid lines: $\phi_{critical} = 0$%, dashed line: $\phi_{critical} = 5$%, and dotted line: $\phi_{critical} = 10$%.

$$\kappa \propto (\phi - \phi_{critical})^3 / (1 - \phi + \phi_{critical})^2, \quad (4)$$

allowing for the existence of a percolation threshold $\phi_{critical}$, the minimum porosity at which fluid can flow through a given porous assemblage [*Sahimi*, 1993]. Results are shown in Figure 5. Given the high porosity of the sandstone, $n = 3$ would be appropriate in equation 3. Instead, this leads to a large underestimation of the permeability increase with porosity. Using $n = 5$ or $n = 7$ narrows the gap between the model and the data, but there is no theoretical basis to justify this, and the fit is still poor. The prediction is not improved if the percolation threshold is increased to 10%.

The observed large change in permeability for a small change in porosity is not predicted by the Kozeny-Carman approach and may result from a combination of increase in connectivity, focused dissolution at the pore throats and/or a reduction in tortuosity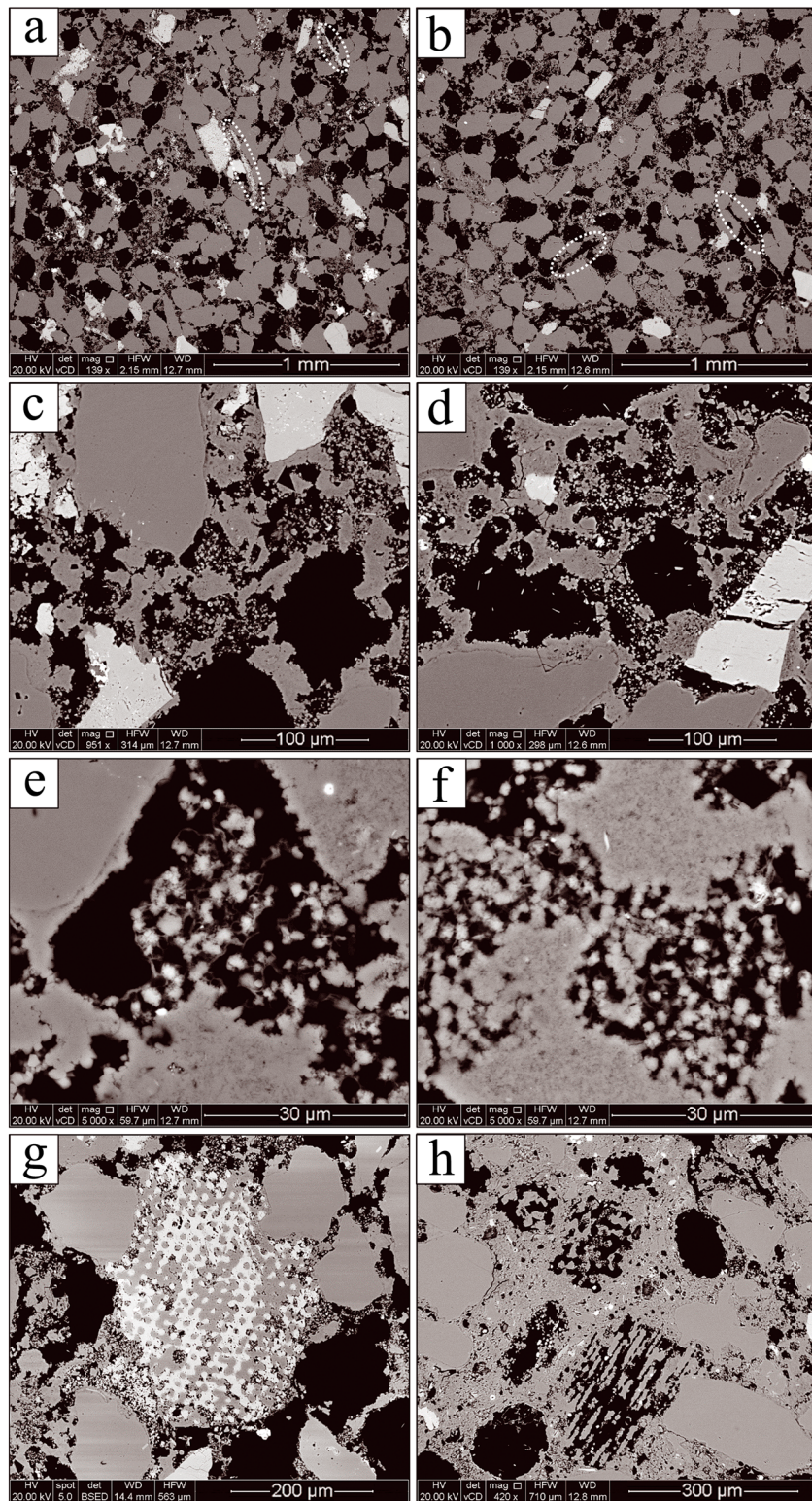. Analysis of micro-CT scans and SEM images of unreacted sandstone (Figures 6a, 6c, 6e, and 6g) suggest that the porosity is already fully connected through numerous small-pore throats so that the dissolution of a few discrete calcite grains would have little effect on the connectivity of the existing pores. No calcite cement was observed at the pore throats (Figures 6c and 6e), and NMR T_2 curves indicate that it is mostly the creation of new large-pore bodies that contributed to the increase in porosity (see Figure S2 of the Supporting Information). Figure 6 contrasts observations made on thin sections of reacted and unreacted cores from a single sample block. From these, we infer that the marked increase in permeability arises primarily from a decrease in tortuosity, as the dissolution of discrete grains opens new flow paths. Calcite shell fragments have dissolved during the experiment creating bridges between preexisting pores, while secondary silicates are apparently unaffected. Random walk simulations have been performed on 3-D models of the pore space reconstructed from separate sets of micro-CT scans (scanner: Scanco microCT 100, pixel resolution: 2.5 µm) following the method described by *Nakashima and Kamiya* [2007]. They show a modest tortuosity decrease from 2.00 to 1.85 due to calcite dissolution, which cannot explain the change in permeability if permeability scales linearly with tortuosity. In our experiments, permeability is more sensitive to tortuosity change because this change results from the opening of new flow paths, not simply a change in sinuosity of existing ones. Therefore, the effect on permeability is fundamentally different from the capillary tube model used as the theoretical basis for K-C based models.

7. Discussion

Our experiments showed that the rate of calcite dissolution in rocks subject to CO_2 injection depends on the rate of transport of acidity to the mineral surface. In practice, this means that the key parameters are the amount of mixing between CO_2 and brine, the local permeability distribution that delivers acidified brine through the rock and the local mineral accessibility. We have also shown that the dissolution of even small amounts of calcite can have a much larger effect on permeability than conventional models predict. Our experiments represent an end member of the conditions likely to be encountered in a steadily filling reservoir because the CO_2 and the brine were mixed prior to injection and the pore volume was refilled with unreacted fluid about a hundred times over the course of the experiment. Nevertheless, this is close to the conditions likely to be encountered in the case of WAG (water alternating gas) injection scenarios.

The advance of acidified brine ahead of a CO_2 plume infiltrating permeable layers may cause significant changes to reservoir permeability, provided that unreacted brines are continually incorporated into the zone of acidification as it moves out from the injection well (radial rather that linear flow). Permeability may also be modified if confining beds above or below a CO_2 plume contain calcite. We believe that there are two key questions for evaluating changes in reservoir performance due to interactions of CO_2-enriched fluid with

Figure 6. SEM images of rock sample (first column) before experiment and (second column) afterward. (a and b) Low-magnification views showing the presence of elongated calcite shell fragments (Figure 6a) matching pores created by the dissolution of such fragments (Figure 6b). (c and d) Details of the pore throat structure showing silicate material coating grains and filling the pores. No significant difference can be detected after the experiments. (e and f) Details of pore fillings (quartz and clay particles) seen in Figures 6c and 6d, confirming that they have been unaffected by the acid brine injection. (g and h) Example of a partly silicified shell fragment (Figure 6g) matched by a comparable pore shape in the reacted sample due to the dissolution of the calcite portion only (Figure 6h).

calcite-bearing rocks. First, how effectively will CO_2 interact with brine, causing acidification and reaction? Second, how effectively will reacted brine pushed ahead of the CO_2 front mix with unreacted brine, creating the potential for further calcite dissolution?

Our results show that it is advisable to evaluate changes in absolute permeability due to fluid-rock interactions since these can lead to variations in effective permeability of similar magnitude to the ones due to phase saturation change. Depending on the specific geological setting, enhanced permeability through calcite dissolution could be a threat to the integrity of injection schemes or could be managed to make them more effective.

References

Andre, L., P. Audigane, M. Azaroual, and A. Menjoz (2007), Numerical modeling of fluid-rock chemical interactions at the supercritical CO_2-liquid interface during CO_2 injection into a carbonate reservoir, the Dogger aquifer (Paris Basin, France), *Energy Convers. Manage.*, *48*(6), 1782–1797, doi:10.1016/j.enconman.2007.01.006.

Bachu, S., and J. J. Adams (2003), Sequestration of CO_2 in geological media in response to climate change: capacity of deep saline aquifers to sequester CO_2 in solution, *Energy Convers. Manage.*, *44*(20), 3151–3175, doi:10.1016/S0196-8904(03)00101-8.

Bachu, S., W. D. Gunter, and E. H. Perkins (1994), Aquifer disposal of CO_2: Hydrodynamic and mineral trapping, *Energy Convers. Manage.*, *35*(4), 269–279, doi:10.1016/0196-8904(94)90060-4.

Bateman, K., C. Rochelle, A. Lacinska, and D. Wagner (2011), CO_2-porewater-rock reactions - Large-scale column experiment (Big Rig II), *Energy Procedia*, *4*, 4937–4944, doi:10.1016/j.egypro.2011.02.463.

Bear, J. (1972), *Dynamics of Fluids in Porous Media*, Elsevier, New York.

Bowker, K. A., and P. J. Shuler (1991), Carbon dioxide injection and resultant alteration of the Weber Sandstone, Rangely Field, Colorado, *AAPG Bull.*, *75*, 1489–1499.

Duan, Z. H., and R. Sun (2003), An improved model calculating CO_2 solubility in pure water and aqueous NaCl solutions from 273 to 533 K and from 0 to 2000 bar, *Chem. Geol.*, *193*(3–4), 257–271, doi:10.1016/j.marchem.2005.09.001.

Hounsfield, G. N. (1973), Computerized transverse axial scanning (tomography): Part 1. Description of system, *Br. J. Radiol.*, *46*(552), 1016–1022, doi:10.1259/0007-1285-46-552-1016.

IEA (2010), Carbon Capture and Storage: Progress and Next Steps, *IEA/CSLF Report to the Muskoka 2010 G8 Summit*.

IPCC (2005), *Carbon Dioxide Capture and Storage*, edited by B. Metz et al., pp. 442, Cambridge Univ. Press, Cambridge, U.K., and New York.

Kharaka, Y. K., D. R. Cole, J. J. Thordsen, E. Kakouros, and H. S. Nance (2006), Gas-water-rock interactions in sedimentary basins: CO_2 sequestration in the Frio Formation, Texas, USA, *J. Geochem. Explor.*, *89*(1–3), 183–186, doi:10.1016/j.gexplo.2005.11.077.

Knauss, K. G., J. W. Johnson, and C. I. Steefel (2005), Evaluation of the impact of CO_2, co-contaminant gas, aqueous fluid and reservoir rock interactions on the geologic sequestration of CO_2, *Chem. Geol.*, *217*(3–4), 339–350, doi:10.1016/j.chemgeo.2004.12.017.

Luquot, L., and P. Gouze (2009), Experimental determination of porosity and permeability changes induced by injection of CO_2 into carbonate rocks, *Chem. Geol.*, *265*(1–2), 148–159, doi:10.1016/j.chemgeo.2009.03.028.

Mavko, G., T. Mukerji, and J. Dvorkin (2003), *The Rock Physics Handbook : Tools for Seismic Analysis in Porous Media*, pp. 339, Cambridge Univ. Press, Cambridge, U.K.

Michael, K., A. Golab, V. Shulakova, J. Ennis-King, G. Allinson, S. Sharma, and T. Aiken (2010), Geological storage of CO_2 in saline aquifers-A review of the experience from existing storage operations, *Int. J. Greenhouse Gas Control*, *4*(4), 659–667, doi:10.1016/j.ijggc.2009.12.011.

Nakashima, Y., and S. Kamiya (2007), Mathematica programs for the analysis of three-dimensional pore connectivity and anisotropic tortuosity of porous rocks using X-ray computed tomography image data, *Int. J. Nucl. Energy Sci. Technol.*, *44*(9), 1233–1247, doi:10.1080/18811248.2007.9711367.

Oelkers, E. H., and D. R. Cole (2008), Carbon dioxide sequestration: A solution to a global problem, *Elements*, *4*(5), 305–310, doi:10.2113/gselements.4.5.305.

Pokrovsky, O. S., S. V. Golubev, and J. Schott (2005), Dissolution kinetics of calcite, dolomite and magnesite at 25 degrees C and 0 to 50 atm pCO_2, *Chem. Geol.*, *217*(3–4), 239–255, doi:10.1016/j.chemgeo.2004.12.012.

Rosenbauer, R. J., T. Koksalan, and J. L. Palandri (2005), Experimental investigation of CO_2-brine-rock interactions at elevated temperature and pressure: Implications for CO_2 sequestration in deep-saline aquifers, *Fuel Process. Technol.*, *86*(14–15), 1581–1597, doi:10.1016/j.fuproc.2005.01.011.

Rosenqvist, J., A. D. Kilpatrick, and B. W. D. Yardley (2012), Solubility of carbon dioxide in aqueous fluids and mineral suspensions at 294 K and subcritical pressures, *Appl. Geochem.*, *27*(8), 1610–1614, doi:10.1016/j.apgeochem.2012.03.008.

Sahimi, M. (1993), Flow phenomena in rocks: from continuum models to fractals, percolation, cellular automata, and simulated annealing, *Rev. Mod. Phys.*, *65*(4), 1393–1534, doi:10.1103/RevModPhys.65.1393.

Sayegh, S. G., F. F. Krause, M. Girard, C. DeBree, and Petroleum Recovery Inst (1990), Rock/fluid interactions of carbonated brines in a sandstone reservoir: Pembina Cardium, Alberta, Canada, *SPE Form. Eval.*, *5*(4), 399–405, doi:10.2118/19392-PA.

Withjack, E. M. (1988), Computed tomography for rock property determination and fluid flow visualization, *SPE Form. Eval.*, *3*(4), 696–704, doi:10.2118/16951-PA.

Xu, T. F., N. Spycher, E. Sonnenthal, G. X. Zhang, L. E. Zheng, and K. Pruess (2011), TOUGHREACT Version 2.0: A simulator for subsurface reactive transport under non-isothermal multiphase flow conditions, *Comput. Geosci.*, *37*(6), 763–774, doi:10.1016/j.cageo.2010.10.007.

Yu, Z. C., L. Liu, S. Y. Yang, S. Li, and Y. Z. Yang (2012), An experimental study of CO_2-brine-rock interaction at in situ pressure-temperature reservoir conditions, *Chem. Geol.*, *326*, 88–101, doi:10.1016/j.chemgeo.2012.07.030.